Chapter 2

Observations and Techniques

The radio observations presented in this thesis were obtained using the Multi-Element Interferometric Radio Linked Network (MERLIN; (Thomasson 1986)) and the Giant Meterwavelength Radio Telescope (GMRT; Swarup et al. 1991). These data sets were supplemented with optical images taken from the *Hubble Space Telescope*, *HST*, archive.

This chapter will initially outline the principles of radio interferometry with particular emphasis on spectral line imaging. Followed by descriptions of the telescopes and interferometers used, along with the data reduction processes employed and details of the individual observations. If a more comprehensive description of the principles of radio interferometry and synthesis imaging are required they can be found in many texts, for example, Taylor, Carilli & Perley (1999) or Thompson, Moran & Swenson (1986).

2.1 The Basic Principles of Radio Interferometry & Aperture Synthesis

If we first consider a single telescope and a radio emitting object. The radio emission from the source can be received by the telescope from a variety of directions surrounding the centre of the field that it is pointed at. However, the efficiency of the antenna (i.e. the power detected) will vary as a function of the distance of the target source from the pointing centre of the antenna. As such, a source that is offset by an angle Θ from the pointing centre will have a detected power which is reduced by a factor of $A(\Theta)$, where $A(0)=1$. Hence the telescope will detect a modified sky brightness distribution,

$$\tilde{I}(\Theta) = A(\Theta)I(\Theta) \tag{2.1}$$

where $\tilde{I}(\Theta)$ tends towards the true sky brightness, $I(\Theta)$, as $\Theta \rightarrow 0$ (close to the pointing centre) but is highly attenuated when Θ is larger than the half power point. Hence, the field of view of the antenna is defined as angular distance from the pointing centre where the radio signal from a source will be attenuated by 50%. This distance is $\sim \lambda/a$ radians, where a is the diameter of the antenna's primary reflector and λ is the observing wavelength and known as the diffraction limit of the antenna.

2.1.1 The Two-Element Interferometer

The basic principle of aperture synthesis (Ryle & Hewish 1960), in which N antennae are linked together to form an array can most simply be thought of as a collection of N(N-1)/2 simple two-element interferometer. Many of the characteristics of a synthesis array can therefore be understood in terms of a collection of interferometer pairs.

Each interferometer pair is formed by correlating (multiplying) the voltage that the two telescopes receive and by integrating this over time, usually a few seconds. The output from a stationary interferometer pair observing a non-variable radio source is known as a *visibility*, V. A visibility approximates to a single Fourier component of the modified sky brightness distribution $\tilde{I}(\Theta)$ in the direction that the telescope is pointed. The interferometer pair is most sensitive to the component of the brightness distribution with the spatial frequency λ/D (=λ/L$\cos\theta$), where λ is the observing wavelength and D (=L$\cos\theta$) is the projected spacing or baseline between the two antennae (see Fig. 2.1).

The projection of the baseline, D, of each pair of antennae onto the plane of the incident wavefront can be described by the orthogonal components *u, v,* & *w*, where *u* represents the direction towards the east, *v* the north and *w* the direction towards the source. Positions on the sky are hence defined in terms of coordinates x and y which are measured as the cosines of these components. These are labelled as Right Ascension (east–west direction) and Declination (north–south direction). Provided the source distribution is not too large, the *w* term can be omitted. Hence, the visibility measured by the interferometer pair can be considered as a sample of the visibility function, V(u, v), where V(u, v) is approximately equal to the Fourier transform of the modified sky brightness distribution $\tilde{I}(\Theta)$.

However, real interferometers are not stationary due to the rotation of the Earth. The projected baseline orientation and length of an interferometer pair is continually changing with time and hence so is the Fourier component of the sky brightness distribution it measures. This fact limits the time over which the visibility can sensibly be integrated over to a period in which this change in the visibility is small.

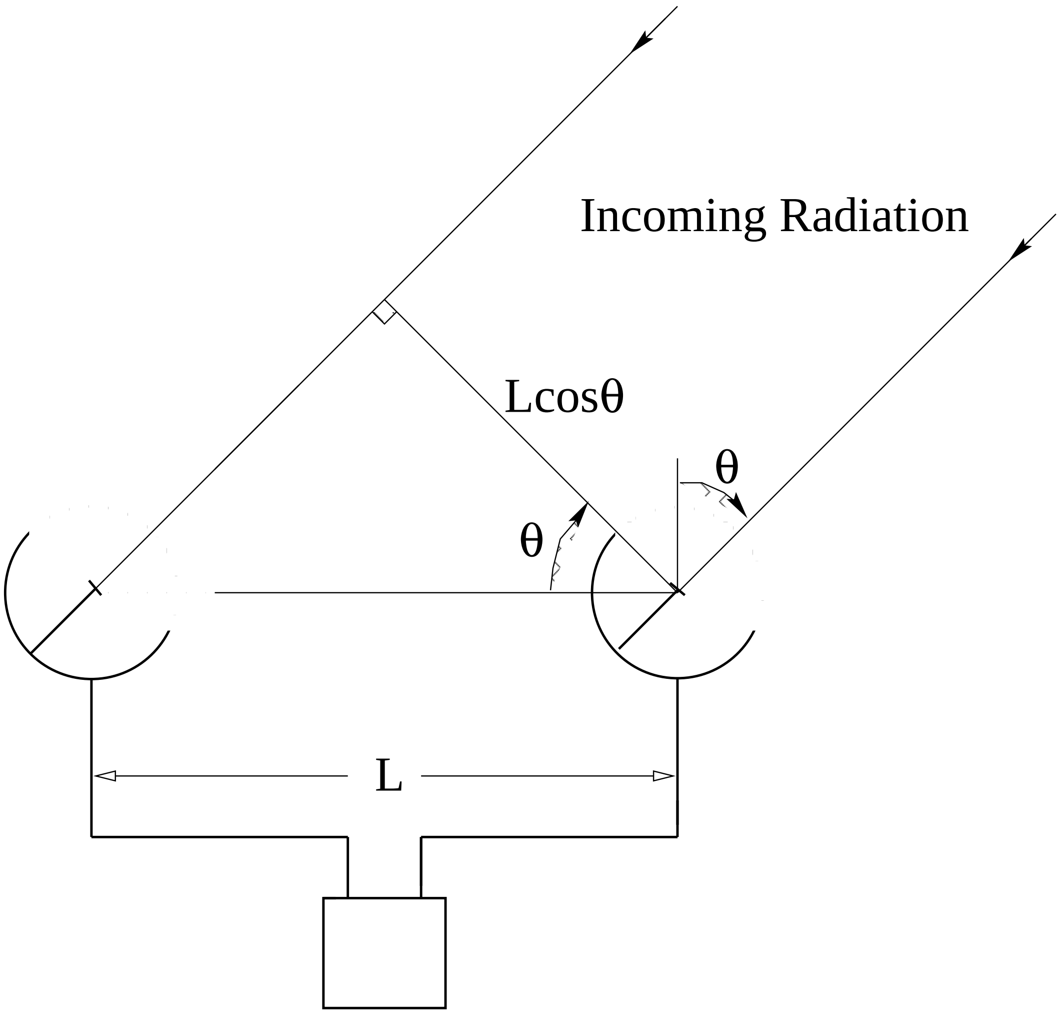

Figure 2.1: A schematic representation of a simple two-element radio interferometer.

2.1.2 Aperture Synthesis

Aperture synthesis utilises the rotation of the Earth. As the Earth rotates, the projected baselines trace elliptical tracks in the u, v plane (see Fig. 2.3 & 2.6), the distribution of sampled points is known as the u, v coverage. A synthesis array detects the spatial frequency components along these tracks and thus samples a portion the Fourier transform, V, of the sky brightness distribution. These sampled visibilities can then be Fourier transformed to recover the sky brightness distribution.

In reality, however, there are many factors that will corrupt the visibilities measured by an interferometer. These include a variety of atmospheric and instrumental effects, which can introduce variations in the amplitude and phase that are not due to the structure of the observed radio source. As a consequence these errors must be determined (calibration process) before the data are Fourier transformed to prevent the creation of spurious source structures.

More fundamentally an aperture synthesis array does not fully sample the u, v plane (i.e. it does not have a filled aperture) which results in a loss of information about the source structure. This effect becomes increasingly evident with sparsely distributed arrays like MERLIN (see section 2.3.1) where relatively small numbers of baselines are used. This loss of information in the Fourier plane introduces sidelobe structures in the point spread function of the observation. The removal of this instrumental response can be achieved using various, non-linear, image processing techniques. The two most commonly used techniques are the Maximum Entropy Method (MEM) and the CLEAN algorithm, both of which will briefly be discussed later in this chapter.

2.2 Calibration

Calibration processes are used to correct for the erroneous contributions to the recorded amplitudes and phases produced by variations in atmospheric conditions or instrumental properties during an observation. Prior to the application of these calibration processes any spurious data points that may be the result of equipment failure or radio frequency interference must be removed or *flagged*. As such, data editing can be considered as an initial stage in the calibration process. The data are viewed as amplitude versus time plots, either for individual baselines or collections of baselines, and any bad data points are removed.

The variations in the measured phase and amplitude result in the observed visibilities, $\tilde{\mathrm{V}}$, being related to the true visibilities by,

$$\tilde{\mathrm{V}}_{ij}(t) = \mathrm{G}_{ij}(t)\mathrm{V}_{ij}(t) \tag{2.2}$$

(Taylor et al. 1999) where G_{ij} is the baseline-based complex gain between antennae i and j, and V is the Fourier transform of the true sky brightness distribution. This baseline-based complex gain can be approximated by the product of the two associated antenna-based complex gain, g_i(t) and g_i(t) where the residual baseline-based complex gain, g_{ij}, is close to 1, this is generally true for a well designed system. Thus

$$\begin{aligned} \mathrm{G}_{ij}(t) &= g_i(t)g_j(t)g_{ij}(t) && (2.3)\\ &\approx g_i(t)g_j^*(t) = a_i(t)a_j(t)e^{i(\phi_i(t)-\phi_j(t))} && (2.4) \end{aligned}$$

where a and ϕ are the antenna amplitude and phase corrections that are to be determined by the calibration process.

Observations of a known point source calibrator, regularly made during the observing run, are used to make a determination of G_{ij} for each of the baselines. The observed response of each baseline to this point source is compared to its expected response to a perfect point source with no phase or amplitude errors. This is then used to determine the phase and amplitude corrections required for each antenna which can then applied to the source data.

In reality, calibrator sources that are compact enough to be used for this purpose generally have a variable flux density. As a result it is necessary to determine the flux density of the point source calibrator observed with respect to a known standard. This is usually provided by a short observation of a source, such as 3C 286, which has a well described, non-varying flux density (Baars et al. 1977; Perley 1990). On long baselines, greater than $\sim 10^4\,\lambda$, the flux calibrator source 3C 286, along with other primary flux density calibrators, is considerably resolved with a subsequent loss of observed flux density. Thus it is necessary to compare the flux density of the point source calibrator and 3C 286 over an appropriate range of baselines. The derived flux density of the point source calibrator can hence be used to calibrate the flux density of all sources observed over the entire range baselines that the interferometer contains.

Time variations in the individual antenna gains, introduced into the signal by the Earth's atmosphere, can cause large phase variations in the radio signal as it passes though the atmosphere with spatial scales of a few degrees and on time-scales that can be as small as a few minutes. The troposhere provides the dominate variations at high frequencies and the ionosphere dominates at frequencies below 5 GHz. In order to calibrate these variations it is essential that short observations of a phase calibrator source, which is close to the target source, are regularly (every 5 – 10 mins) made between observations of the target. It is not essential that this phase calibration source be unresolved on all baselines of the interferometer as long as it contains enough compact structure to be visible over all of the baselines. In some cases (primarily bright target sources) it is also possible to exploit the technique of self-calibration in which the target source is itself, used to derive the phase corrections needed; this will be discussed later in this section.

It should be noted that for spectral line observations, the amplitude and phase corrections are generally determined from using data formed by averaging the observed spectral channels over the entire observing bandwidth with the prior removal of any bad channels (usually channels near to the edges of the passband).

Bandpass Calibration

The baseline-based complex gains also vary with frequency. These result in frequency dependent variations of the amplitude and phase due to the differing amplitude response of the receiver across the observing band. This effect also needs to be corrected for in the calibration process.

To remove these frequency based variations a bright calibrator source (bandpass calibrator), with a flat spectrum over the spectral band of interest, is observed. It is reasonable to assume that the visibilities recorded from this source are identical in each observed channel regardless of frequency. Assuming this, the required bandpass correction can be determined and then applied to the source data.

It is vital to gain a good bandpass calibration if high sensitivity spectral line observations are to be made. Ideally the calibration source should be observed for long enough so that the bandpass calibration does not add significantly to the noise. This will depend upon the continuum flux of the target source and the bandpass calibrator. Hence longer observations of the same bandpass calibrator will be required for a brighter target source, such as a radio galaxy, than for a weaker target, such as a weak Seyfert galaxy.

Self–Calibration Techniques

The technique of self-calibration can be used to improve the quality of the calibration solutions following the application of the solutions derived from the phase calibrator. In some circumstances it can even be used to calibrate the data when no phase calibration source has been observed. This technique uses an initial model of the source intensity distribution to calibrate the residual telescope gains (Cornwell & Wilkinson 1981). At each iteration of the self-calibration cycle a new map is made from the newly corrected data which can then be used as an improved model and re-inputed into the next cycle of self-calibration. This process is repeated until the calibration is not significantly improved by further iterations. This technique is possible because the individual residual telescope gains can be determined for each baseline, such that for N telescopes there are N(N-1)/2 baselines and hence N(N-1)/2 equations can be used to solve the individual telescope errors. An individual telescope error is fixed and all others are assigned relative to it and therefore all of the N-1 unknown telescope errors can be solved using N(N-1)/2 equations.

2.2.1 Imaging & Deconvolution

Following calibration, the *u, v* data can be Fourier transformed to create an image of the source. This process is done in image reduction packages, such as AIPS, by first interpolating the data into a rectangular grid and then applying a fast Fourier transform (FFT). The incomplete sampling of the *u, v* plane by the interferometer can be considered as a sampling function where grid squares that contain data are assigned to be unity and those that do not are considered to be zero. In effect this means that the true source visibility is multiplied by a sampling function. The point source response to this sampling function is known as the *dirty beam*. The *dirty beam* contains complicated sidelobe structures that arises as a consequence of the Fourier transform of the incompletely sampled visibility distribution. Likewise, the Fourier inversion of the source visibilities is known as the *dirty map* and is the true brightness distribution of the source convolved with the *dirty beam*.

There are two commonly used non-linear deconvolution techniques that correct for the defects in the *dirty map*, CLEAN (Högbom 1974) and the Maximum Entropy Method, or MEM (Gull & Daniell 1978; Cornwell & Evans 1985). The CLEAN deconvolution algorithm assumes that the source can be represented by a number of point sources in an otherwise empty field. The algorithm finds these point sources and iteratively subtracts a scaled *dirty beam* from each of these points, starting with the brightest. The final image, following this deconvolution process, is known the CLEAN image and is formed from the sum of these point sources convolved with a Gaussian beam. MEM, on the other hand, finds the smoothest possible positive map that, to within the noise level of the experiment, fits the data by maximising the entropy in the map. MEM is subsequently more suited to sources that contain smooth extended structure.

2.2.2 Weighting

During the imaging process it is necessary to assign each cell in the gridded data a weight based upon the observed values (Briggs, Schwab & Sramek 1999). The two most extreme, and most commonly used, weighting schemes are natural and uniform weighting. In natural weighting, each cell is given a weighting according to the number of measured data points within that cell. As a result, this scheme will give heavier weight to areas of the u, v coverage that are more densely sampled, usually towards the centre of the u, v distribution. Thus the natural weighting scheme provides the highest sensitivity but at the expense of the angular resolution. In the uniform weighting scheme each cell is given the same weight irrespective of the number of data points it contains. This scheme will give more emphasise to the sparsely sampled cells at the edges of the u, v distribution (corresponding to longer baselines) and hence will generally provide a higher resolution than natural weighting. However, the uniform scheme gives the same weight to cells that contain either many or very few data points thus this scheme tends to reduce the sensitivity of the resulting image compared to natural weighting.

In addition, to natural and uniform weighting schemes, it is also possible to weight the data using an intermediate scheme. Intermediate weighting schemes can be used to try and optimise the final image and reduce the compromise between resolution and sensitivity that exists in the two extreme schemes. Throughout this thesis both uniform and natural weighting schemes have been employed as well as a variety of intermediate schemes with the choice of weighting being dictated by the scientific goals.

2.2.3 Resolution and Observable Structure

The maximum angular resolution that is obtainable from a radio interferometer is determined by the maximum baseline length and the frequency of the observation. This maximum resolution is in effect the synthesised beam of the instrument. If the interferometer is used to observe a source that has a smaller angular size than the synthesised beam, the radio interferometer will act like a single dish and measure an intensity distribution of a point source broadened to the beam size. Similarly, radio interferometers are also unable to detect sources that are larger than the smallest fringe spacings provided by the antennae distribution. Any structure larger than the fringe spacing of the shortest baseline will be severely attenuated. These two factors dictate the size range of structures that a radio interferometer can detect. For example an observation with MERLIN (maximum baseline 217 km and minimum baseline 6.4 km) at λ=20 cm will be able to detect radio structure on angular scales between the synthesised beam size of $\sim0.''15$ and the maximum observable source size of $\sim6.''5$.

This effect is unique to interferometers and the lost information cannot be regained during the reduction process. The combination of a data set made from a similar observation of the target using a different interferometer can be used to regain some of this missing information. For example, combining an observation made with MERLIN with one made using the VLA, which has many shorter baselines, will provide shorter fringe spacings and enable larger scale structures to be observed. Similarly, MERLIN observations (and/or VLA observations) may be combined with higher resolution VLBI observations to increase the maximum resolution, with the MERLIN baselines providing the short fringe spacings. This technique increases the range of fringe spacings (u, v coverage) sampled and hence improves the image quality.

2.2.4 Spectral Line Imaging

Spectral line imaging is the natural extension to the basic concept of spatial imaging to include a third dimension, namely frequency. A typical spectral line (example of an absorption line is shown in Fig. 2.7) can be described by,

$$S(\nu) = S_c + S_l(\nu, \nu_0, \mathrm{A}, \Delta\nu) \qquad \text{where} \quad \Delta\nu \ll \nu_0 \tag{2.5}$$

where $S(\nu)$ is the observed spectral energy distribution at frequency ν, S_c is the source's continuum component which is assumed to be independent of frequency and S_l describes the source's line component. The line component S_l is characterised by the line amplitude, A, width (FWHM), $\Delta\nu$, and central frequency ν_0.

For a spectral line observation to fully determine these line characteristics it must have a bandwidth that is wide enough to include the entire line along with some of the adjacent continuum emission. The observation must also have adequate spectral resolution to determine the line width and central frequency to an accuracy dictated by the scientific goals of the experiment.

The observing band is split into a large number individual, narrow-bandwidth, spectral channels which span the width of the spectral line being observed and some of the adjacent continuum. Each spectral line channel can be subsequently considered in a similar manner to a continuum band observation producing a two dimensional image of the radiation received at a specific frequency (*channel map*) but with a considerable narrower bandwidth than a standard spatial imaging experiment. The frequency resolution of a spectral line observation is determined by the width of these individual channels. These channels should be narrow enough to separate different source regions at different radial velocities. All of the channel maps that make up the entire observation can be stacked together to create a three dimensional data '*cube*' with two spatial axes and one frequency axis.

It is necessary to take considerable care when deconvolving spectral line data cubes using CLEAN because this algorithm can create artifacts and errors that are proportional to the strength of the source. The result is that these artifacts can dominate the noise levels and compromise the dynamic range that can be obtained, especially when observing strong continuum sources. However, this can be overcome by removing the continuum emission before CLEANing the spectral line data (also see section 2.4.3).

The Relationship Between Frequency and Velocity

The frequency of a given spectral line observation can be related to radial velocity via the Doppler equation if the rest frequency of the spectral line and its observed frequency are known. Including the relativistic correction this can be equated as,

$$\frac{v}{c} = \frac{\nu_0^2 - \nu^2}{\nu_0^2 + \nu^2} \tag{2.6}$$

where v is the radial velocity of the observed spectral line, ν_0 is the rest frequency of the line, ν is the observed frequency of the line and c is the speed of light. There are two commonly used methods for approximating equation 2.6 when $v \ll c$. In the radio definition, this approximation is,

$$\frac{v_{\mathrm{radio}}}{c} = \frac{\nu_0 - \nu}{\nu_0}. \tag{2.7}$$

Whereas in the optical definition the frequencies are replaced with wavelengths and the approximation is given as,

$$\frac{v_{\mathrm{optical}}}{c} = \frac{\lambda - \lambda_0}{\lambda_0}(\equiv z) \tag{2.8}$$

$$= \frac{\nu_0 - \nu}{\nu} \tag{2.9}$$

where z is the source redshift. The optical and radio velocity conventions are easily convert between using the equation,

$$\frac{v_{\mathrm{radio}}}{v_{\mathrm{optical}}} = \frac{\nu}{\nu_0}. \tag{2.10}$$

It is important to note that both of these conventions are extensively used but can give significantly different results. Throughout this thesis, all radial velocities have been calculated using the optical convention applied to the heliocentric rest frame. All the sources presented in this thesis have redshifted velocities of less than 14000 $\mathrm{km\,s^{-1}}$ and hence the non-relativistic approximations are valid.

2.3 Radio Interferometers used for Observations Presented in this Thesis

2.3.1 MERLIN

The majority of the observations presented in this thesis were taken with Multi-Element Radio Linked Interferometric Network (MERLIN, Thomasson 1986).

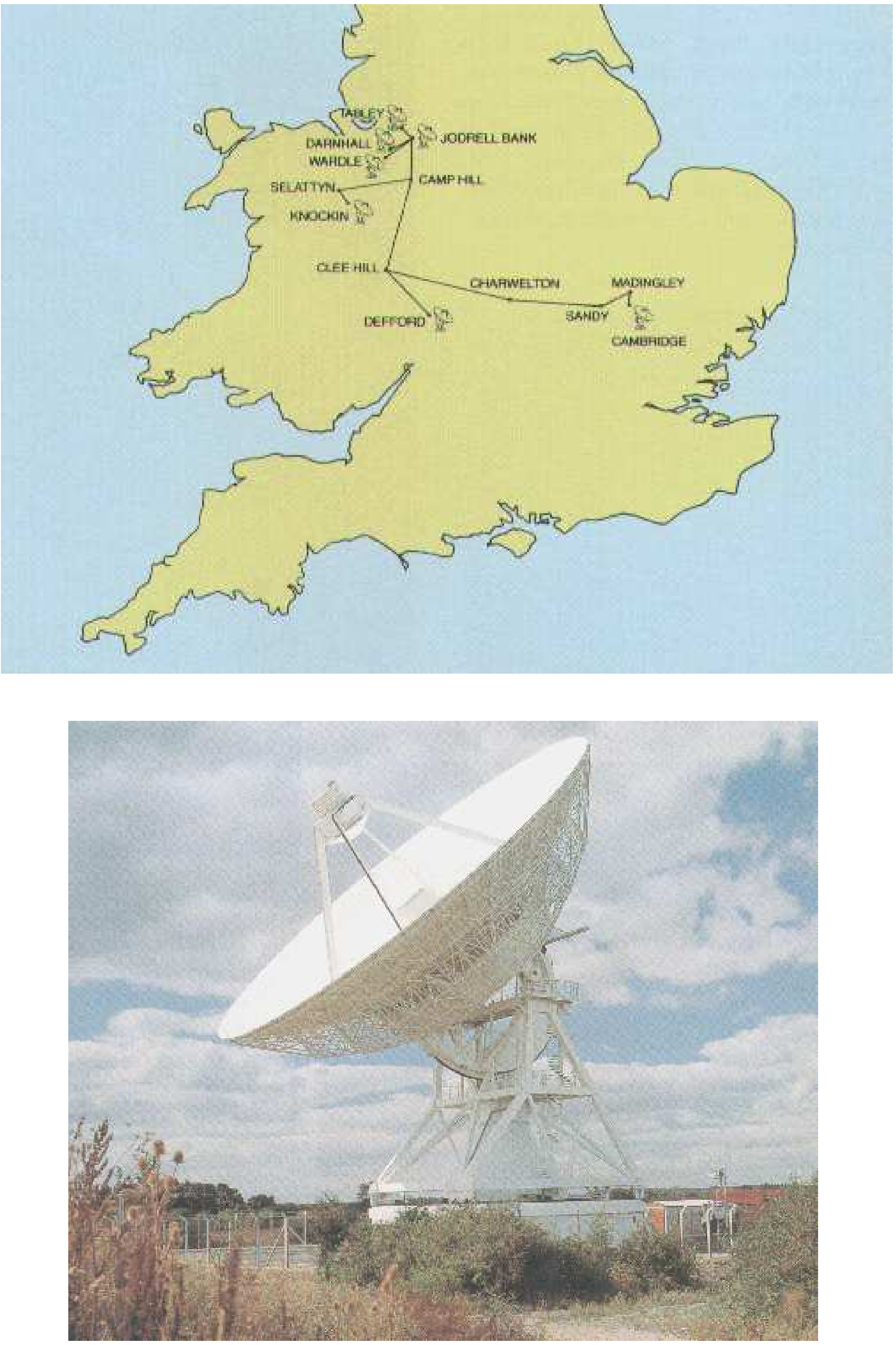

Figure 2.2: Upper: Map showing the location of the MERLIN telescopes and microwave links. Lower: A representative picture of one of the MERLIN telescopes, the 32-m diameter telescope at Cambridge (taken from www.jb.man.ac.uk, Photograph taken by Keith Papworth).

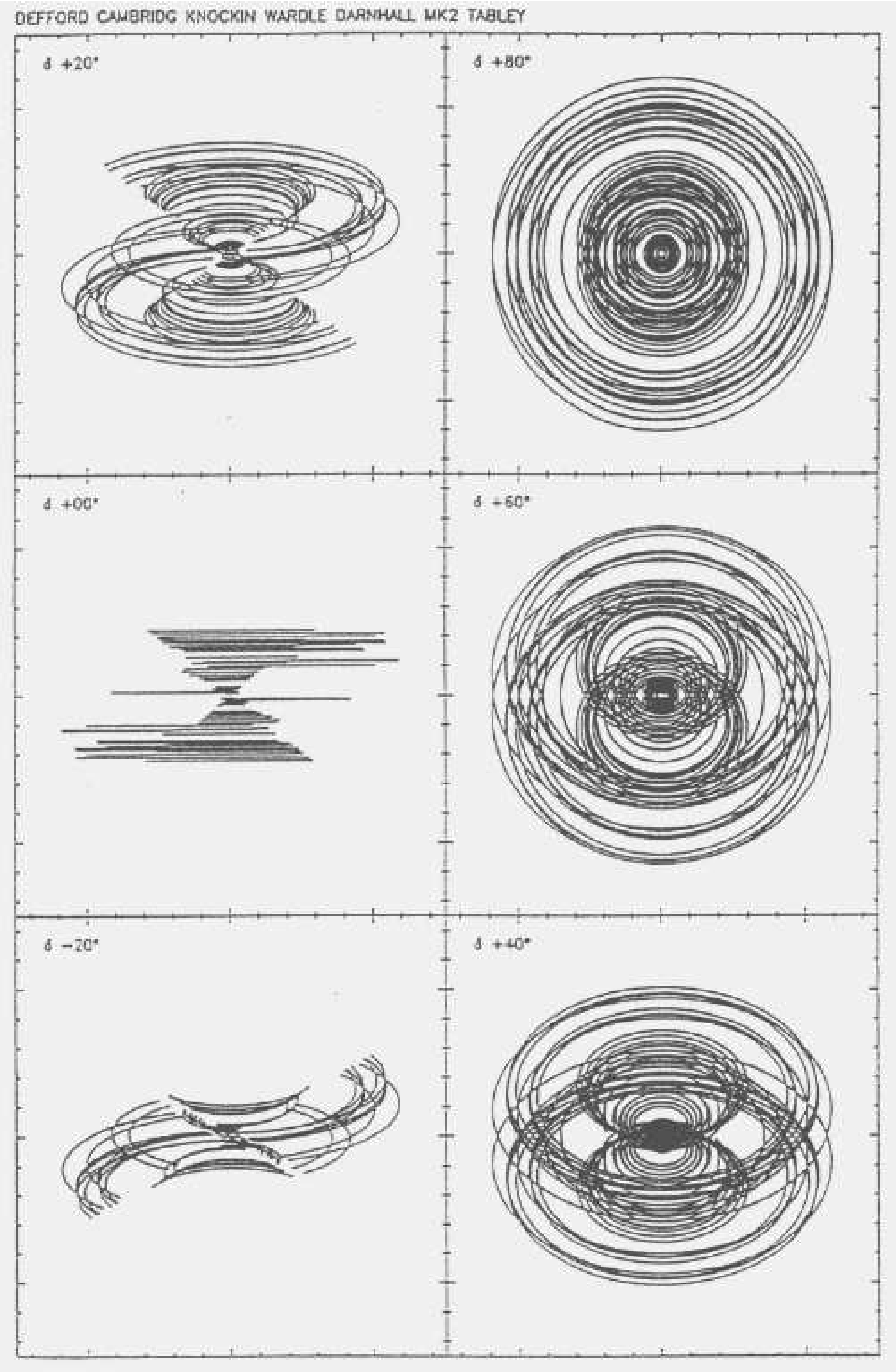

Figure 2.3: The u, v coverage of MERLIN for 7 telescopes at a variety of sources declinations. The long tick marks are at intervals of 10 Mλ (from MERLIN User Guide).

MERLIN is an irregularly spaced aperture synthesis array that consists of 7[1] inhomogeneous (76-m to 25-m diameter) individual telescopes spread across the southern part of the UK (see Fig. 2.2).

Unlike other aperture synthesis arrays, such as the VLA the relatively sparse u, v coverage of MERLIN (see Fig. 2.3) results in a less complete sampling of the Fourier components that represent the sky brightness distribution. Consequently MERLIN is reliant upon the rotation of the Earth to synthesise a useful aperture and is rarely used with a 'snapshot-type' observing strategy.

2.3.2 The GMRT

The Giant Meterwavelength Radio Telescope (GMRT[2], Swarup et al. 1991) is an aperture synthesis instrument consisting of 30 fully steerable 45 metre diameter parabolic antennae located at Khodad near Pune in India (19°05′ N and 74°03′ E). Since the GMRT was designed as a low frequency instrument each of the antennae uses a light weight wire mesh based construction to form the reflecting surface (see Fig. 2.4). The wire mesh is held in place by a series of steel rope trusses, Stretched Mesh Attached to Rope Trusses (SMART), which pull the mesh into a series of flat surfaces which approximate to a parabola. The size of the wire mesh used is varied across the reflecting surface, with three gauges of mesh each covering a third of the surface area. The smallest sized (10 mm) mesh is used in the central region of the parabola with the largest (20 mm) used towards the edges. This results in each antenna having a tapered illumination pattern which reduces the sidelobe levels of each antenna's primary beam. The RMS deviations of each antenna away from an ideal parabola is 8, 9, 14 mm at each of the three

[1]Some of the older observations presented in this thesis also include the use of the Wardle telescope which is not presently part of the MERLIN array.

[2]Current information about the status of the GMRT is available from www.ncra.tifr.res.in.

Figure 2.4: Photograph of two of the thirty GMRT antennae.

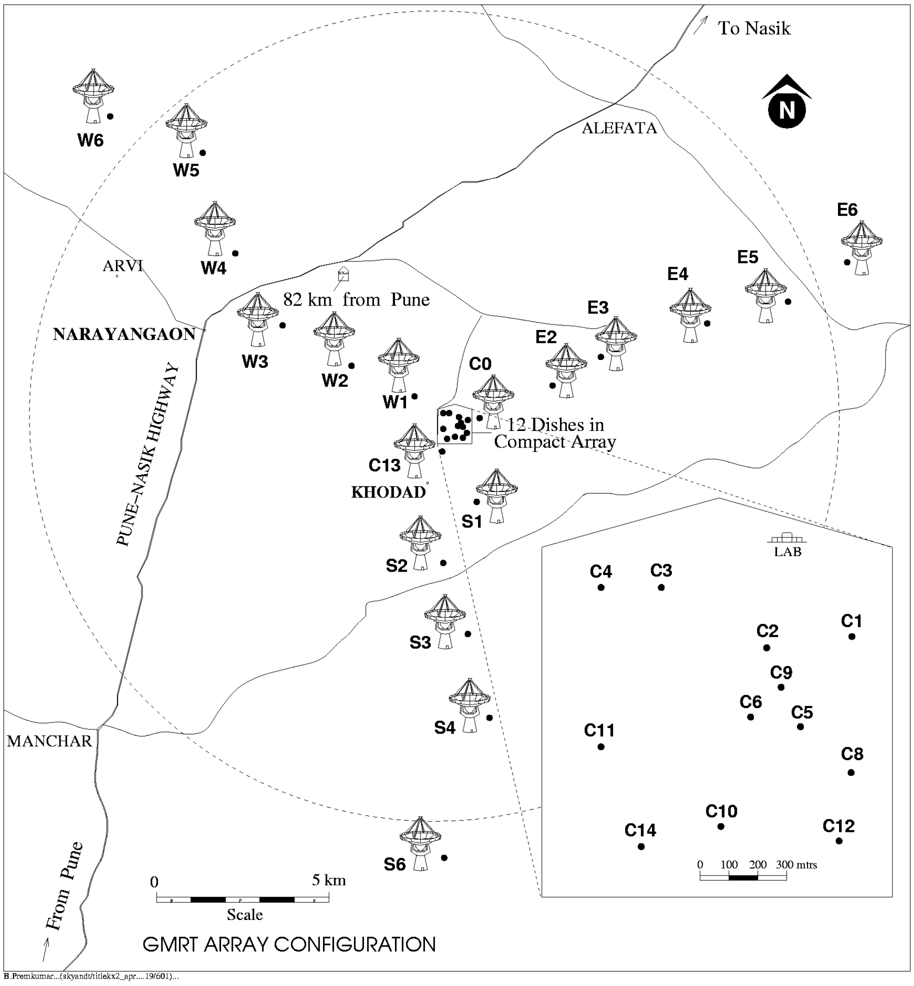

Figure 2.5: Map showing the distribution of the 30 telescopes that form the GMRT (From GMRT documentation available at www.ncra.tifr.res.in).

different wire mesh regions (Bhatnaga 2001).

The GMRT array is irregularly distributed with 12 antennae (see Fig. 2.5) situated in a compact central cluster, called the '*central square*'. The baselines within the '*central square*' range between ~100 m and ~1 km. The remaining antennae are located along three arms forming an approximately 'Y' shaped array with baseline lengths of up to 25 km (see Fig. 2.5). The 1420 MHz feeds, used in the observations presented in this thesis, consist of broadband corrugated horns with the ability to observe over the frequency range of 900→1450 MHz continuously.

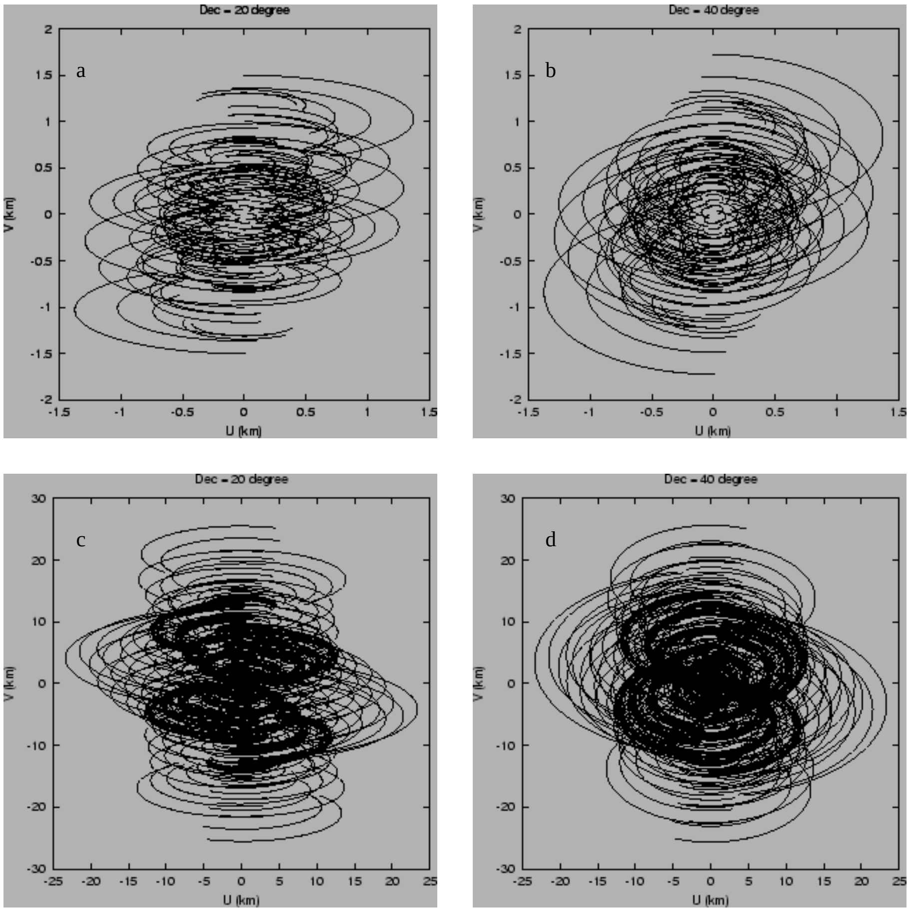

Figure 2.6: The u, v coverage for the GMRT over a 12 hour integration at various source declination. a) Central square at declination +20 degrees. b) Central square at declination +40 degrees. c) Full GMRT array at declination +20 degrees. d)Full GMRT array at declination +40 degrees.

The FWHM of the primary beam of each of the GMRT antennae is $\sim 25''$

The GMRT observations presented in chapters 3 and 4 of this thesis were observed in a one week period in November 2000 whilst this telescope was still in a testing and development stage. These observations were the first science observations to be made with GMRT by any astronomer not directly collaborating with institutes involved in the construction of this telescope.

2.4 Data Reduction

2.4.1 Preliminary MERLIN Data Reduction

The initial evaluation, editing and calibration of MERLIN data were carried out using the MERLIN DPROGS software package, developed by Simon Garrington and Neal Jackson at Jodrell Bank Observatory.

Gain–elevation corrections for the individual telescopes in the MERLIN array were initially applied to the data. These are needed to account for the variations in sensitivity of each of the individual antennae as a function of elevation due to differing values of air-mass, ground spillover radiation and atmospheric absorption. These corrections were applied using pre-tabulated information for each antenna at the stipulated observation wavelength.

DPLOT was then used to view the amplitudes and phases of each of the MERLIN baselines against time. This allowed initial assessment of the data quality and provided a simple way in which bad data points could be edited. Bad data points were edited either using this facet of DPLOT or following this initial processing stage within NRAO's Astronomical Image Processing System (AIPS).

In addition to any bad data points that result from external factors such as the weather or radio frequency interference the Lovell telescope is incapable of driving with adequate speed (time-scales $\sim$1 minute) between the source and phase calibrator to enable phase calibration to be successfully achieved. The MERLIN observing strategy overcomes this by leaving the Lovell telescope on-target for the majority of the observations and only uses it to observe the phase calibration source every few observing cycles. This strategy results in an observed effect, known as the 'Lovell drop-out', since the target source is normally significantly weaker in amplitude than the phase calibrator. Prior to further data reduction procedures this effect was edited from the data.

Flux Density Calibration of Point Source Calibrators

The flux density scale for each observation was determined for individual, unresolved, point source calibrators (i.e. has the same observed amplitude on all MERLIN baselines) using an observation of the flux density calibrator 3C 286. To avoid resolving out the extended structure of 3C 286, the relative observed amplitudes of 3C 286 and the point source calibrator were recorded only on the three shortest MERLIN baselines (Tabley–Darnhall, Tabley–Mark II and Darnhall-Mark II). The flux density of 3C 286, which varies with frequency, was determined using the DFLUX program which interpolates the known flux density values for the source for a specified frequency. This relationship between the unresolved flux density of 3C 286 and observing frequency is described by equation 2.11,

$$\log \mathrm{S} = 1.480 + 0.292\log\nu - 0.124(\log\nu)^2 \tag{2.11}$$

(Perley, Schwab & Briddle 1986).

Auto–voltage correlation (AVC) corrections which correct for the contribution of the sky brightness and the source to the recorded flux density for each baseline were calculated using the program DAVC. These corrections were applied to the measured amplitudes of 3C 286 and the point source calibrator using an assumed sky brightness temperature of 3 K. The final flux density of the point source calibrator, $\mathrm{S_{PS}}$, for each baseline were calculated from the known values of 3C 286, $\mathrm{S_{3C\ 286}}$, with the relevant AVC corrections (α_{PS} and $\alpha_{\mathrm{3C\ 286}}$) for each baseline applied as follows,

$$\mathrm{S_{PS}} = \mathrm{S_{3C\ 286}} \times \frac{\mathrm{A_{PS}}\alpha_{\mathrm{PS}}}{\mathrm{A_{3C\ 286}}\alpha_{\mathrm{3C\ 286}}} \tag{2.12}$$

where A_{PS} and $A_{3C\ 286}$ are the amplitudes recorded for each of the calibrators. A final value for the flux density of the point source calibrator was then obtained by averaging the values determined for each of the three shortest baseline.

Each of the MERLIN data sets were then calibrated to a reference antenna (Mark II) and the correlator gains were averaged using the TDPROC program. TDPROC produces a data file comprising of all of the observed sources in the FITS file format which was loaded into AIPS where further data reduction processes were applied.

2.4.2 Reduction and Analysis – AIPS

The AIPS package was used for all further data reduction of both continuum and spectral line radio interferometry data. The initial reduction and imaging of MERLIN data, within AIPS, was carried out using an automated pipeline developed by Tom Muxlow. Data from other radio instruments, such as the GMRT, were also reduced within AIPS employing similar data reduction routines as used in this automated pipeline (described below) but applied manually (also described in NRAO's AIPS Cookbook[3]).

The MERLIN pipeline was used to initially load the pre-edited, multiple source FITS file into AIPS. AIPS tasks were then applied to create bandpass and phase calibration solutions which were applied to the amplitude calibrated source data. Both the calibrators and sources were then imaged and successive iterations of self-calibration and re-mapping were cycled through to increase the signal-to-noise of the resulting maps, for the sources with had adequate brightness. Throughout the application of the automated pipeline postscript files of the calibration solutions and images of the sources were produced allowing constant monitoring of this part of the reduction process.

[3]Latest editions are available at http://www.cv.nrao.edu/aips/cook.html.

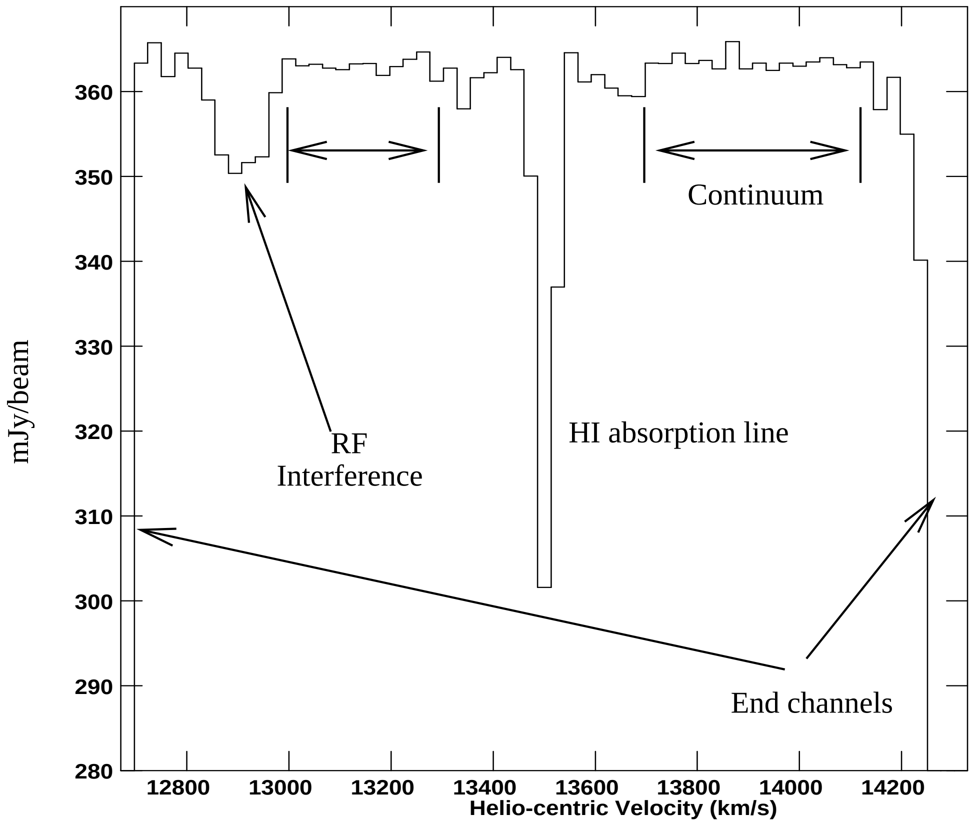

Figure 2.7: An example of a HI absorption spectra obtained with an interferometer showing the full bandwidth of the observation used. Both HI absorption and radio-frequency interference can be seen. (Source is 3C 293, further details of this data set are given in chapter 3).

2.4.3 The Special Case of Spectral Line Data Reduction

As was briefly stated earlier, spectral line imaging has some similarities to continuum spatial imaging but with the added degree of difficulty that results from a third dimension. The majority observations presented in this thesis are spectral line observations and in particular observations of the 21 cm line of neutral hydrogen in absorption.

The reduction techniques for spectral line data initially follow a very similar method to that of spatial imaging, with the exception of the application of a bandpass calibration (see section 2.2). The primary difference in the calibration techniques for spectral line observations is that, whereas continuum observations contain a relatively large observed bandwidth sampled by a small number of channels that are usually averaged together at an initial stage, spectral line observations contain many spectral channels. These spectral channels are required to provide the frequency information that is often the primary purpose of the observations. In practice, spectral line data that have been phase referenced are averaged together following a bandpass calibration to form the equivalent of a continuum data set, thus reducing the noise levels compared with a single spectral channel, and calibrated in an analogous manner to a continuum data set. These calibration solutions can then be applied to the non-averaged spectral line data set. This greatly reduces the computational time required in calculating individual calibration solutions for each spectral line channel.

The deconvolution of spectral line data sets also requires greater care than continuum data sets. In particular it is necessary to subtract the radio continuum and clean the line data separately (see section 2.2.4). The subtraction of the continuum data can either be performed in the image or u, v planes (Rupen 1999). For the majority of the observations presented in this thesis continuum subtraction was applied in the image plan, although subtraction in the u, v plane was also used. Continuum subtraction in the u, v plane using AIPS tasks such as UVLSF or UVLIN can give superior results for data which requires high dynamical ranges. Subtraction in the u, v plane also results in simplification of the process when the continuum is split over several groups of channels compared with the subtraction of the continuum in the image plane.

All of the MERLIN spectral line observations in this thesis were made using an 8-MHz bandwidth that was split into either 64 or 128 correlator channels, resulting in a channel width of 125-kHz or 62.5-kHz (corresponding to a velocity width

Source	NGC 6240(1)	NGC 6240(2)
Interferometer	MERLIN	MERLIN
Date of Observation	18/19 May 2000	30/31 May 2000
Approximate length of observation	$\sim$8 hours	$\sim$8 hours
Position (B1950)	$16^{h}50^{m}27^{s}.8$ $02^{\circ}28'\ 58''.5$	$16^{h}50^{m}27^{s}.8$ $02^{\circ}28'\ 58''.5$
Observing Frequency	4994 MHz	4994 MHz
Calibrators		
Amplitude	3C 286	3C286
Point	2134+004	2134+004
Phase	1648+015	1648+015

Table 2.1: Observing parameters for the radio continuum observations that are presented in this thesis.

of $\sim$26 km s^{-1} or $\sim$13 km s^{-1}). Observations using the GMRT were also made using an 8-MHz bandwidth and were correlated into 128 channels. The central channel of each of the observations was centred upon the systemic velocity of the observed source to ensure that the spectral line was centred towards the middle of the band. The exception to this was the observation of NGC 7674 which was observed at a slightly erroneous systemic velocity resulting in the absorption line being situated towards the beginning of the band (for details see chapter 4).

The third axis of the imaged spectral line data cubes were transformed from frequency to velocity in the optical-heliocentric convention, following the equations stated in section 2.2.5, using the AIPS tasks ALTDEF and ALTSWCH.

Subsequent Data Cube Analysis

A variety of AIPS tasks were used to extract information about the kinematics and abundances of neutral hydrogen from the spectral line cubes. Maps of the individual channels were formed from the continuum subtracted data cubes to show the spatial distribution of the neutral hydrogen absorption at particular velocities. These individual channel maps were combined along the velocity axis to produce maps of the integrated distribution of HI over the source (*moment 0* map). Furthermore these data were also used to derive maps of the velocity distribution (*moment 1* map) from the intensity weighted velocity average and to map the distribution of the observed line width (*moment 2* map). In addition, slices through the data cubes along various axes were used to produce position-velocity images allowing detailed inspection of velocity gradients within the HI gas against the target sources.

The opacities, column densities and line profiles of the HI absorption against the individual radio continuum components were derived from spectra obtained using the task ISPEC. Gaussian fitting to the spectral lines using the AIPS task SLFIT was used to determine the radial velocities and FWHM of the spectral lines. The optical depth, τ, of HI against each radio continuum component was calculated by summing the individual optical depths within each channel over the width of the absorption line. The optical depth in each channel was determined from the absorption line intensity, $\mathrm{T_L}$, and the level of the continuum intensity, $\mathrm{T_C}$ using,

$$\tau = -\ln \frac{\mathrm{T_C} - \mathrm{T_L}}{\mathrm{T_C}}. \tag{2.13}$$

The HI column densities were calculated using this derived opacity and assuming an electron spin temperature of 100 K (see section 1.4.1).

2.5 Radio Observations

The details of all of the radio observations that are presented in this thesis are summarised in Tables 2.1, 2.2 & 2.3. These tables present the various observing parameters used for both the MERLIN continuum observations (Table 2.1) and the spectral line observations made using the GMRT, MERLIN and global VLBI arrays (Table 2.2, & 2.3).

2.6 Optical Observations – HST

The *Hubble Space Telescope, HST*, was launched into a low earth orbit (~600 km) in 1990 and has become one of, if not, the most successful optical telescope project of the last decade. The telescope consists of a 2.4-metre reflecting telescope which due to its location, above the Earth's atmosphere, produces defraction limited results with a resolution of ~0.1 arcsec. In 1993, a service mission to correct for the, well documented, spherical aberration problems caused by the misalignment of the primary mirror was successfully completed. This servicing mission was also used to install new instrumentation such as the Wide Field & Planetary Camera 2 (WFPC-2). The *HST* data policy requires that all data over one year old become publicly accessible through the *HST* archive (http://archive.stsci.edu). WFPC-2 images obtained from the *HST* archive have been used to compare with MERLIN data throughout this thesis (see Tab. 2.5).

The WFPC-2[4] instrument consists of 4 charge couple devices, three f/12.9 wide field camera chips with a pixel size of $0.09959\pm0\farcs00002$ and one high resolution planetary camera with a pixel size of $0.04553\pm0\farcs00004$.

[4]Detailed information on the capabilities and status of the WFPC-2 instrument can be found at http://www.stsci.edu/instruments/wfpc2/.

Source	**3C 293**	**3C 293**	**3C 293**	**NGC 7674**
Interferometer	GMRT	MERLIN	VLBI+	GMRT
No. of antennae	30	8	50+	30
Date of observation	Nov. 11-12th 2000	Apr. 8th 1998	– 1998–2001	Nov. 12th 2000
Approximate length of observation	12h	18h	–	10h
Position (B1950)	$13^{h}50^{m}3^{s}.21$ $31°41'\ 33''.0$	$13^{h}50^{m}3^{s}.21$ $31°41'\ 33''.0$	$13^{h}50^{m}3^{s}.21$ $31°41'\ 33''.0$	$23^{h}25^{m}24^{s}.41$ $08°30'\ 12''.5$
Spectral line	HI	HI	HI	HI
No. of channels	128	64	–	128
Channel width (kHz)	62.5	125	125	62.5
Cen. $V_{opt-hel}$ ($km\,s^{-1}$)	13500	13500	13500	8725
Calibrators				
Amplitude	3C 286	3C 286	3C 286	3C 286
Phase	1347+122	OQ208	OQ208	2212+018
Bandpass	1347+122	OQ208	OQ208	2212+018

Table 2.2: Observing parameters for the spectral line observations that are presented in this thesis (continued in the next table). VLBI+ represents combined data sets from Global VLBI, MERLIN and VLA (plus Pie Town) observations. These VLBI+ observations are presented and commented upon in chapter 7.

Source	**NGC 7674**	**NGC 7469**	**NGC 6240**	**NGC 6240**
Interferometer	MERLIN	MERLIN	MERLIN	MERLIN
No. of antennae	7	7	7	6
Date of observation	Nov. 12th 2000	May 10th 1996	Jan. 31st 1998	Jan. 12th 1998
Approximate length of observation	10h	8h	11h	10h
Position (B1950)	$23^{h}25^{m}24^{s}.41$ $08°30' 12''.5$	$23^{h}00^{m}44^{s}.41$ $08°36' 15''.9$	$16^{h}50^{m}27^{s}.8$ $02°28' 58''.5$	$16^{h}50^{m}27^{s}.84$ $02°28' 58''.5$
Spectral line	HI	HI	HI	H_2CO
No. of channels	64	64	64	64
Channel width (kHz)	125	125	125	125
Cen. $V_{opt-hel}$ ($km\,s^{-1}$)	8725	4843	7300	7300
Calibrators:-				
Amplitude	3C 286	3C 286	3C 286	3C 286
Phase	2325+093	2306+095	1648+015	1648+015
Bandpass	OQ208	0552+398	0552+398	OQ208

Table 2.3: Observing parameters for the spectral line observations that are presented in this thesis (cont.).

Source	III Zw 35	UGC 2369	IR 0335+015	Zw 49.0
Interferometer	MERLIN	MERLIN	MERLIN	MERLIN
No. of antennae	7	7	7	7
Date of observation	Nov. 10-11th 2000	Nov. 11-12th 2000	Dec. 4th 2000	Nov. 11th 2000
Position (B1950)	$01^h41^m47^s.90$ $16°51'\ 06''.0$	$02^h51^m15^s.91$ $14°46'\ 04''.5$	$03^h35^m58^s.73$ $15°23'\ 03''.6$	$15^h10^m45^s.69$ $07°24'\ 42''.4$
No. of channels	128	64	64	128
Polarisations	LL	LL & RR	LL & RR	LL
Channel width (kHz)	62.5	125	125	62.5
Cen. $V_{opt-hel}$ ($km\,s^{-1}$)	8175	7981	10710	3901
Calibrators:-				
Amplitude	3C 286	3C 48	3C 286	3C 286
Phase	0136+176	0249+171	0341+158	1509+054
Bandpass	0552+398	0249+171	0552+398	0552+398

Table 2.4: Observing parameters for the HI absorption observations that are presented in chapter 6 of this thesis (cont.).

Source	**3C 293**	**NGC 7674**	**NGC 7469**	**NGC 6240**
Dataset	U27I5A01A	U5DF0201B	U33Z1901A	U4GE0101B
Filter	F702W	F547M	F219W	F814W
Filter characteristics				
Central λ (Å)	6940	5446	2117	8203
$\Delta\lambda$(Å)	1480.6	486.6	367.9	1758.0
Integration time	280 sec	200 sec	2×1200 sec	1200 sec

Table 2.5: Observing parameters for the *HST* data sets that are presented in this thesis.

2.6.1 Data Reduction

Prior to the transfer of data from the *HST* archive a calibration pipeline was applied to the WFPC-2 data which corrects for dark currents, flat fielding etc. Following the receipt of the data the only remaining data reduction process that had to be achieved was the cleaning of the images of contaminating cosmic rays. These data were processed using the Space Telescope Science Data Analysis System (STSDAS) within the Image Reduction and Analysis Facility (IRAF[5]) and using some software packages developed by the UK's STARLINK[6] project, such as KAPPA.

The further analysis of individual data sets, including the highly problematic task of the registration of *HST* and images with radio data, are described in detail in the relevant chapter.

[5]Information about the IRAF suit of reduction programs is available on the world wide web at http://iraf.noao.edu.

[6]Information about the STARLINK project is available on the world wide web at http://star-www.rl.ac.uk/.